Vacancy-type defects and their trapping/detrapping of charge carriers in ion-implanted GaN studied by positron annihilation

Akira Uedono[1], Ryo Tanaka[2], Shinya Takashima[2], Katsunori Ueno[2], Masaharu Edo[2], Kohei Shima[3], Shigefusa F. Chichibu[3], Jun Uzuhashi[4], Tadakatsu Ohkubo[4], Shoji Ishibashi[5], Kacper Sierakowski[6], and Michal Bockowski[6]

[1]*Division of Applied Physics, Faculty of Pure and Applied Science, University of Tsukuba, Tsukuba, Ibaraki 305-8573, Japan*

[2]*Advanced Technology Lab., Fuji Electric Co., Ltd., Hino, Tokyo 191-8502, Japan*

[3]*Institute of Multidisciplinary Research for Advanced Materials, Tohoku University, Sendai 980-8577, Japan*

[4]*National Institute for Materials Science, Tsukuba 305-0047, Japan*

[5]*Research Center for Computational Design of Advanced Functional Materials (CD-FMat), National Institute of Advanced Industrial Science and Technology (AIST), Tsukuba, Ibaraki 305-8568, Japan*

[6]*Institute of High Pressure Physics, Polish Academy of Sciences, Sokolowska 29/37, 01-142 Warsaw, Poland*

Annealing behaviors of vacancy-type defects in ion-implanted GaN were studied by positron annihilation. Mg^+ and N^+ ions were implanted to obtain 700-nm-deep box profiles with Mg and N concentrations of 1×10^{18} cm^{-3}, and the samples were annealed using an ultra-high pressure annealing system. For as-implanted samples, the major defect species was identified as Ga-vacancy (V_{Ga})-type defects. For N-implanted GaN, the size

of the vacancies increased as the annealing temperature increased up to 1100°C and then shrinked above 1200°C. This behavior was attributed to recombinations between N-vacancy (V_N)-type defects and excess N. For Mg-implanted GaN, the major defect species after annealing above 1000°C was vacancy clusters such as $(V_{Ga}V_N)_3$. Some of them acted as nonradiative recombination centers for blue and ultraviolet luminescence. Their energy levels corresponding to the transition from positive to neutral were located between 2.6 eV above the valence band maximum and the conduction band minimum. The thermal activation process of electron detrapping from the vacancy clusters was also studied. For Mg-implanted GaN, one of the major secondary defects was collapsed vacancy disks forming dislocation loops. They were eliminated by additional N-implantation, which was associated with vacancy agglomerations under the annealing in V_{Ga}-rich condition.

1. Introduction

Silicon carbide (SiC) and gallium nitride (GaN) have been recognized as key materials for post-Si power electronics [1,2]. Compared with traditional devices such as Si-based metal-oxide semiconductor field-effect transistors (MOSFETs) and insulated gate bipolar transistors, SiC- and GaN-based devices can operate at a higher power and higher frequency because of their excellent physical properties [3,4]. Using these widegap semiconductors, one can also decrease the on-state resistance and increase the breakdown voltage, which results in a reduction in energy loss during their device operation. The differences in the fundamental properties of SiC and GaN, however, make one a better fit than the other in their applications. SiC is mainly used for devices that offer a high voltage ($\geq$ 1 kV) with a high current-carrying capability [2,5]. This makes it a good fit for applications such as inverters for automobiles, trains, solar farms, etc. On the other hand, GaN is mainly used for devices operating at a relatively low voltage ($\leq$ 0.6–0.65 kV) [4]. Their typical applications are consumer electronics such as power converters, motor drivers, wireless power transfer, telecommunication servers, etc.

At present, almost all commercial GaN devices are made with a lateral architecture [2,4]. In this structure, two-dimensional electron gas (2DEG) is generated at a few nanometers far from the AlGaN/GaN heterojunction on the GaN side due to spontaneous and piezoelectric effects. 2DEG is often influenced by imperfections near the AlGaN/GaN interface such as traps, charged defects, and interface roughness, and they degrade the device properties. There is continuous demand for the breakdown voltage of GaN-based devices to be increased, and this can be done by increasing the distance between the gate and the drain. This solution, however, would degrade the device performance due to the effects of interface imperfections. In contrast, the vertical device

architecture can offer distinct advantages such as a higher current density and breakdown voltage [6,7]. In this structure, the current vertically flows from the surface to the epitaxial GaN layers, and the electric field peaks can be set away from the surface, which improves the device breakdown voltage and reliability.

Because of the recent progress on growth technology for bulk GaN [8–10], high-performance vertical GaN diodes and transistors have been demonstrated, and the breakdown voltage of such devices was reported to be higher than 1 keV [7,11–18]. Several different architectures for vertical devices have been proposed, such as a planer-type vertical MOSFET (or double-implanted MOSFET, DMOSFET), vertical channel field-effect transistors, junction barrier Schottky diodes, etc. Here, optimization of the device processing is key for commercializing vertical devices. One of critical building blocks is the selective area doping of impurities. For example, control of the acceptor concentrations in the p-well of DMOSFETs is critical because it determines the threshold voltage. The precise control of impurity concentrations and their profiles can be done using only ion implantation. Edge termination such as field-limiting ring and junction termination extensions is a common technique that separates the peak electric field from the surface. Because this structure is formed using ion implantation for Si- and SiC-based devices, the same process is desired for GaN-based devices.

The major drawback of ion implantation is the generation of high-concentration point defects due to atomic collisions [19]. It is well known that activation of Mg implanted into GaN is more difficult than that of Si or Ge [7,20]. This has been associated with the presence of donor-like point defects such as nitrogen vacancies (V_N) because they act as compensators. In this context, additional implantation of N or F atoms into Mg-implanted GaN is considered to be effective to enhance the activation rate of implanted Mg [15, 21].

The sequential implantation of N was reported to be also effective to suppress the diffusion of Mg during post-implantation annealing [15,22]. Another key technology for the fabrication of p-type GaN using ion implantation is post-implantation annealing. Because the surface of GaN starts to decompose above 1000°C, the annealing is usually done for samples with a surface protective layer such as AlN, SiO_2, SiN, etc. However, even using such layers, the highest annealing temperature is limited to be around 1300°C [7,20]. Several annealing techniques have been applied to decrease thermal budgets, such as microwave annealing, rapid thermal annealing (RTA), multicycle RTA, laser annealing, etc. [23–26]. A rather straightforward approach to suppress the degradation of GaN during annealing is ultra-high-pressure annealing (UHPA) [7,27,28]. UHPA can anneal GaN up to 1480°C under a N_2 pressure of 1 GPa without the need to form a protection layer. Using UHPA, it has been reported that the activation rate of Mg exceeded 70%, and the carrier mobility was close to that of epitaxially grown p-type GaN [7,27].

Although ion-implantation is an effective process for fabricating vertical GaN devices, the reactions of point defects and the formation process of secondary defects, such as dislocations, precipitates, and stacking faults, are not well known. The presence of such defects could relate to the degradation of electric properties and the reliability of devices. In addition, although the control of dopant profiles is crucial, they could be affected by the interaction between implanted dopants and point defects. Thus, knowledge on the annealing behaviors of point defects is important. Positron annihilation spectroscopy is a useful technique for detecting vacancy-type defects in solids [29,30]. This technique has been used to study native and process-induced defects in GaN [22,31–39]. In the present study, we used a monoenergetic positron beam to study the annealing

behaviors of vacancy-type defects in Mg- and N-implanted GaN. The electron trapping by such defects and their release process were also studied. Optical properties and secondary defects for the samples were studied by photoluminescence (PL) and scanning transmission electron microscope (STEM).

2. Experimental

The samples used in the present experiments were undoped 4-μm-thick GaN films grown on GaN substrates by metal-organic vapor phase deposition (MOVPE). The substrates in the *c*+-direction were grown by hydride vapor phase epitaxy (HVPE). Mg^+ ions were implanted with energies of 10 to 700 keV to obtain a 700-nm-deep box profile with a Mg concentration ([Mg]) of 1×10^{18} cm^{-3}. The total dosage of Mg was 9.7×10^{13} cm^{-2}. After the Mg-implantation, N^+ ions were implanted with energies of 20 to 600 keV in order to know effects of sequential implantation of N on annealing properties of defects. The depth profile of N was set to be similar to that of Mg, and the N concentration in the box profile was 1×10^{18} cm^{-3}. The total dosage of N was 9.1×10^{13} cm^{-2}. N^+ ion-implanted samples without Mg-implantation were also prepared, where the implantation condition was the same as that for the sequential N-implantation. All ion implantations were performed at room temperature (RT). After the implantation, the samples were annealed at temperatures between 1000°C and 1450°C for 5 minutes under a N_2 pressure of 1 GPa using a UHPA system [40].

The depth distributions of the Mg in the samples were measured by secondary ion mass spectrometry (SIMS). For the Mg-implanted samples with and without N-implantation, photoluminescence (PL) spectra were measured using a 325-nm line of a He-Cd laser with a power density of 38 W/cm^2. The measurements were performed at 13

K and RT. The samples were also characterized by an aberration-corrected scanning transmission electron microscope (STEM, FEI Titan G2 80-200). A low-angle annular dark-field (LAADF) STEM observation was used to obtain images of secondary defects in these samples.

Vacancy-type defects in the ion-implanted samples were probed using a monoenergetic positron beam. Details on this technique are given elsewhere [29]. The Doppler broadening spectra of the annihilation radiation were measured using Ge detectors as a function of the incident positron energy E. The spectra were characterized by the S parameter, which was defined as the fraction of annihilation events over the energy range of 510.22–511.78 keV. The relationship between the S parameter and E was analyzed by the computer code VEPFIT [41]. Using the coincidence technique [29], Doppler broadening spectra were also measured and characterized by the S and W parameters. The W parameter was defined as the number of annihilation events in the energy ranges of 504.14–507.96 keV and 514.04–517.86 keV. The Doppler broadening spectra were measured in darkness and under the illumination of a 325-nm He-Cd laser (Kinmon Koha, IR3802R-G). The relationship between the S parameter and the photon energy of the illumination was measured using a monochromator with a Xe lamp (Bunkoukeiki, SM-5).

The Doppler broadening spectra were simulated by QMAS (Quantum MAterials Simulator) code [42] based on the projector augmented-wave (PAW) method [43] and a plane-wave basis set. In the calculation, an orthorhombic cell equivalent to the $4 \times 4 \times 2$ hexagonal unit cell of a wurtzite structure was used. In this super cell structure without vacancies, the number of atoms was 128. The Perdew–Burke–Ernzerhof-type generalized gradient approximation [44] was used to express the electronic exchange-correlation

interaction. Atomic positions were computationally optimized by evaluating the Hellmann-Feynman force. Details on the application of QMAS to calculations of positron states and annihilation parameters in group-III nitrides are given elsewhere [45,46].

3. Results and Discussion

3.1 Annealing behaviors of vacancies in N-implanted GaN

Figure 1 shows the *S* values of the N-implanted GaN before and after annealing as a function of *E*. The mean implantation depth of positrons is shown on the upper horizontal axis. The dotted line shows the *S* value corresponding to the annihilation of positrons from the delocalized state (0.442) [22,47]. For the as-implanted sample, the *S* values at *E* = 2–12 keV were almost constant and higher than the *S* value for the delocalized state, suggesting the trapping of positrons by vacancy-type defects introduced by N-implantation. The large *S* value at $E \cong 0.1$ keV is due to the annihilation of positrons at the surface. The *S* value for the damaged region was increased by annealing up to 1100°C, and it then started to decrease above 1200°C annealing. For the sample annealed at 1400°C, the *S* value was higher than that for the delocalized value, suggesting that the vacancy-type defects remained even after annealing at 1400°C.

The solid curves shown in Fig. 1 are fits to the experimental data. In the fitting procedure, the region scanned by positrons was divided into two or three blocks. The *S* value for each block and the position of blocks were determined by the fitting. Figure 2 shows the derived depth distributions of *S*. The depth profile of N was calculated by using SRIM code [48], and the result is also shown in Fig. 2. For the as-implanted sample, the depth profiles of vacancy-type defects and N agreed well each other. With the increase in

annealing temperature, the vacancy profile shifted toward the surface. Above 1100°C annealing, the S values near the surface (< 100–300 nm) were larger than those in the deeper damaged region (400–700 nm), suggesting the agglomeration of vacancy-type defects and their migration toward the surface. From the results for the sample annealed at 1400°C, residual defects were found to exist in the region at ≤ 600–700 nm. Figure 3 shows the annealing behavior of the S value measured by the coincidence Doppler broadening technique at E = 5 keV. It shows that the shrinkage of the vacancy size (decrease in the S value) started above 1200°C annealing. The effect of illumination on the S value will be discussed later.

Figure 4 shows S–W plots for the N-implanted GaN before and after annealing, which were obtained from the coincidence Doppler broadening spectra (brown and pink symbols). The value of E was fixed at E = 5 keV. Because the mean implantation depth of positrons at this energy is about 70 nm, the (S,W) value mainly corresponds to the annihilation of positrons in the damaged region (see Fig. 2). The statistical errors of the (S,W) values are close to the size of the symbol used in the figure. The (S,W) value corresponding to the positron annihilation in a delocalized state is shown as "DF" (defect-free). The (S,W) value calculated from the simulated Doppler broadening spectrum for the delocalized state is shown as "DF(cal.)." The simulated (S,W) values for the vacancy-type defects, such as the Ga-vacancy V_{Ga}, and their complexes with V_N [$V_{Ga}(V_N)_n$, $(V_{Ga}V_N)_2$, and $(V_{Ga}V_N)_3$, (n=1–3)] are also shown in Fig. 4 (blue symbols).

For the as-implanted sample (as-imp.), the (S,W) value measured in darkness was close to the values for V_{Ga} and $V_{Ga}V_N$. Considering the difference between the S values obtained by experiments and simulations for the delocalized state, the major defect species in the as-implanted sample can be identified as V_{Ga}-type defects. A similar defect

species was reported to be introduced for H- and Si-implanted GaN before annealing [22,47,49]. After annealing at 1000–1100°C, the (*S*,*W*) value shifted to the right-hand side. The simulated (*S*,*W*) value for vacancy clusters [$(V_{Ga})_m(V_N)_n$] tended to shift toward the right-hand side as m or n increased. Thus, the observed shift in (*S*,*W*) can be attributed to the agglomeration of vacancy-type defects. After 1200°C annealing, however, the (*S*,*W*) value shifted towards the left-hand side, and the values for the samples annealed at 1300 and 1400°C were located on the line (brown) connecting the values for DF and the sample before annealing. From the observed annealing behavior of the (*S*,*W*) value, it can be concluded that the shrinkage of vacancy-type defects starts above 1200°C, and this can be attributed to recombinations between vacancy clusters and excess N atoms. After annealing at 1300 and 1400°C, the major defect species is not considered to be that much different from that for the as-implanted sample, but their concentration was lower than that before annealing.

Using the two-state trapping model [29], the concentration of the residual vacancies was estimated from the *S* values experimentally obtained for the positron annihilation from the delocalized state and the sample annealed at 1400°C. The characteristic value of *S* for the residual vacancies was assumed to be the average of the *S* values simulated for V_{Ga} and $V_{Ga}V_N$. Assuming that (i) the trapping rate of positrons of such defects is that for neutral divacancy for Si (2×10^8 cm^3s^{-1}, ref. 26) and (ii) the lifetime of positrons annihilating from the delocalized state is the one obtained for HVPE-GaN (0.15 ns, ref. 48), the defect concentration was estimated to be 2×10^{17} cm^{-3}. The present result suggests that N sequential implantation is effective to suppress the agglomeration of vacancies and their concentration, but one needs to anneal the sample at least above 1200°C to obtain this effect.

3.2 Vacancy-type defects in Mg-implanted GaN

Figures 5 and 6 show *S*–*E* plots for the Mg-implanted GaN and the derived depth distributions of *S*, respectively. Figure 6 also shows the depth distributions of Mg measured by SIMS for the samples after annealing at 1300°C and 1400°C. There was no large change in the Mg profile below 1300°C annealing [47]. Unlike the annealing behavior of *S* for the N-implanted sample, the *S* value corresponding to the annihilation of positrons in the damaged region started to decrease above 1100°C annealing (see Fig. 3). In Fig. 6, for the samples before annealing and after annealing at below 1100°C, the damaged region (≤ 700 nm) agreed with the box profile of Mg. After annealing at 1400°C, the *S* value corresponding to the box profile of Mg (0–700 nm) was close to that for the delocalized state, suggesting that the concentration of vacancies detectable by positron annihilation was under the detection limit (≤ 10^{15} cm^{-3}, ref. 26).

Figure 7 shows the *S*–*W* relationship for the Mg-implanted sample. For the as-implanted sample, the major defect species can be identified as V_{Ga}-type defects. Above 1000°C annealing, all the (*S*,*W*) values were close to the line connecting the values for DF(cal.) and $(V_{Ga}V_N)_3$, suggesting that the major defect species was vacancy clusters such as $(V_{Ga}V_N)_3$. After above 1300°C annealing, the (*S*,*W*) values were close to the value for DF. With the increase in annealing temperature, Mg could be partially activated. As a result of a downward shift in the Fermi level position, the charge states of vacancy-type defects could change from neutral to positive (ex. $V^0 \rightarrow V^+$). Because positrons are repelled from positively charge defects, they are not detected by positron annihilation [29]. This is an origin of the decrease in *S* (increase in *W*) shown in Figs. 5–7 [22,47,49].

3.3 Trapping/detrapping of charge carriers by vacancy clusters in ion-implanted GaN

Figure 8 shows the *S*–*E* curves for N-implanted GaN after annealing at (a) 1000°C and (b) 1200°C and those for Mg-implanted GaN after annealing at (c) 1000°C and (d) 1100°C. These measurements were performed in darkness and under illumination using a He-Cd laser. The depth distributions of *S* for these samples are shown in Fig. 9. For these samples, the *S* values corresponding to the damaged region were increased by the illumination, suggesting the increase in the trapping rate of positrons by vacancy-type defects. The photon energy (3.8 eV) of the He-Cd laser is higher than the bandgap of GaN. Thus, electrons were excited from the valence band to the conduction band by the illumination, and they could be trapped by positively charged vacancy clusters (i.e. $V^+ + e^- \rightarrow V^0$). For the N-implanted sample, the illumination effect was not observed before the annealing (Fig. 3). This suggests that positively charged vacancies are formed after annealing. As the annealing temperature increases (≥ 1200°C), the concentration of positively charged vacancies is considered to decrease. For the Mg-implanted sample after annealing above 1300°C, the effect of the illumination was also diminished. For this sample, partially activated Mg is considered to have trapped the electrons generated by the illumination and suppress their trapping by vacancies.

Figures 4 and 7 show the (*S*,*W*) values measured under illumination for N- and Mg-implanted GaN, respectively. For the N-implanted samples (Fig. 4), illumination caused a right-hand shift in the (*S*,*W*) values. Because the simulated (*S*,*W*) value for $V_{Ga}(V_N)_n$ tends to shift towards the right-hand side as n increases, the illumination active vacancy clusters are likely to have a higher number of V_N compared with neutral (or negatively

charged) ones. For the Mg-implanted sample (Fig. 7), illumination caused a bottom-right shift in the (*S*,*W*) values. This movement in the diagonal direction is due to the shift in the (*S*,*W*) values toward the value of the delocalized state in darkness. Thus, the similar defect species [$(V_{Ga})_m(V_N)_n$, m < n] is considered to be an origin of the change in the (*S*,*W*) value by illumination.

Figure 10 shows (a) PL spectra for the Mg-implanted GaN after annealing at 1100°C. Measurements were performed at 13 K and RT. The relationship between photon energy of illumination and the *S* value at *E* = 5 keV for the same sample is also shown in Fig. 10(b). In the PL spectrum measured at 10 K, an observed sharp luminescence peak at 3.46 eV and an ultraviolet luminescence (UVL) band have been associated with the recombination of excitons bound to a Mg (Mg_{Ga}) acceptor (acceptor bound excitons: ABEs) and a free electron or shallow donor to Mg_{Ga} transition, respectively [51–53]. A blue luminescence (BL) band has been assigned to deep donor and Mg_{Ga} acceptor pair (DAP) recombinations [52,54]. These peaks and bands suggest that implanted Mg atoms are partially activated after annealing at 1100°C. The emissions from deep energy states such as green luminescence (GL) and red luminescence (RL) bands have been associated to V_N-related defects [51–55]. For the PL spectrum measured at RT, a broadened yellow luminescence (YL) band was observed. For Mg-implanted GaN, YL is a common emission band, and it has been attributed to a DAP recombination between a donor impurity such as oxygen at a nitrogen site (O_N) and V_{Ga} [55,56], where oxygen is the major impurity of MOCVD-grown GaN. The near-band-emission (NBE) peak is broadened, and its intensity is low, which is also typical for ion-implanted GaN, and it can be attributed to the presence of defects introduced by ion implantation [55].

As shown in Fig. 10(b), the *S* value started to increase above 2.6 eV, and it saturated

above the band gap energy of GaN (3.4 eV). This suggests that the electron trapping of vacancy clusters occurs in this energy range, and their energy levels are located in the NBE region. In this energy range (2.6–3.4 eV), BL and UVL emissions are suppressed in the PL spectrum measured at RT. Thus, the decrease in their emission can be associated with vacancy clusters that act as nonradiative recombination centers as well as exciton dissociation.

Figure 11 shows the time dependences of the S value measured at E = 5 keV for the Mg-implanted GaN annealed at 1100°C before and after illumination of a He-Cd laser. The measurements were performed in (a) wide and (b) narrow time ranges. For the latter measurements, laser pulses were created using a mechanical shutter, and the measurements of Doppler broadening spectra were synchronized with pulse cycles. Dotted lines show the S value before illumination. The value of S was 0.4715 in darkness, and it was increased by the illumination. After the illumination, the S value immediately dropped to ~0.475, but its full recovery required about 10 h [shown as a dotted line and vertical arrows in Fig. 11(a)]. The recovery of the S value after the illumination can be associated with the thermal activation of electrons from the trapped state of vacancy clusters.

The S–t relationship shown in Fig. 11(b) was fitted to the equation $S(t) = S_0F(t) + S_F[1 - F(t)]$, where S_0 and S_F are the S values of the initial and final states (0.4715). $F(t)$ is an empirically based stretched exponential function, known as the Kohlrausch-Williams-Watts (KWW) function, $F(t) = \exp[(-t/\tau)^{\beta}]$, where τ and β are the time constant and the stretching exponent, respectively [57–59]. The solid curve is the result of the fitting, and the values of τ and β were derived to be 0.17 ± 0.05 h and 0.17 ± 0.02, respectively. The KWW function is often used as a phenomenological description of

dynamics in solid-state materials. When it is used to fit current transients of electric devices, for example, the time dependence of the current could originate from more than one deep level and/or mini-bands of carrier traps, etc. [59]. In the present case, the obtained β value (< 1) suggests that there is more than one thermal activation path for charged vacancy clusters. As shown in Fig. 11(a), the electron emission from the vacancy clusters continued for hours.

3.4 Effects of sequential N-implantation on vacancies in GaN

For Mg-implanted GaN with N-implantation, the annealing behavior of *S* was measured by using the coincidence Doppler broadening technique at $E = 5$ keV, and the result is shown in Fig. 3. The measurements were done in darkness and under illumination. No large difference between the annealing behaviors for the samples with and without N-implantation was observed. After annealing above 1300°C, however, the *S* values for the sample with N-implantation were slightly higher than those for the sample without N-implantation. Figure 12 shows the *S*–*E* curves for Mg-implanted GaN with and without N-implantation after annealing at 1450°C. The inset shows the depth distributions of *S* for these samples. The *S* values in the subsurface region ($E = 5$–15 keV) were higher than the *S* value for the delocalized state, and the depth distributions of vacancies (≤ 600 nm) agreed with the box profiles of Mg for the samples before annealing. This fact suggests that the vacancies remain even after annealing at 1450°C. For the sample with N-implantation, the *S* value corresponding to the damaged region was higher than that for the sample without N-implantation, suggesting that the additional N-implantation increased the concentration of residual defects that were detectable using positron annihilation.

Figure 13 shows PL spectra for the Mg-implanted GaN with and without N-implantation after annealing at 1450°C. For the sample with the N-implantation, the emission intensity of ABE was higher than that for the sample without the N-implantation, suggesting an increase in activated Mg concentration and/or a decrease in the concentration of midgap recombination centers (MGRC) [55]. In the PL spectrum measured at RT, GL was suppressed for the sample with N-implantation, which can be attributed to the recombination between V_N-type defects and excess N atoms. However, the *S*–*W* plot for the Mg-implanted GaN with N-implantation showed no clear difference from that for the samples without N-implantation (not shown). The lack of the effect of sequential N-implantation on the (*S*,*W*) value could be attributed to two reasons. Because V_N-type defects are not an effective trapping center of positrons, positron annihilation is rather insensitive to the change in their concentrations. The additional implantation of N introduces not only V_N-type defects but also vacancy clusters. Thus, excess N atoms might be consumed by the recombination with V_N-type defects introduced by both Mg- and N-implantation, and the rate of recombination with other vacancies could be suppressed.

Figure 14 shows LAADF-STEM images of the (a) N-implanted GaN, (c) Mg-implanted GaN, and (e) Mg-implanted GaN with N-implantation. Their magnified images are shown in Figs. 14(b), 14(d), and 14(f), respectively. These images were taken for the samples after annealing at 1400°C. For the N-implanted sample [Fig. 14(a) and (b)], bright dots were observed. Their origin has been attributed to nano scale intrinsic defects and dislocation loops [60–62]. For the Mg-implanted sample [Fig. 14(c) and (d)], bright dots and circles were observed. The nature of the latter defects was identified as a collapsed vacancy disk forming an intrinsic dislocation loop [60–62]. For the Mg-

implanted GaN with N-implantation, the formation of dislocation loops was suppressed [Fig. 14(e) and (f)].

For the samples with and without N-implantation, since a certain number of vacancy-type defects exists even in high temperature annealing, they must affect the formation process of secondary defects. For the sample with N-implantation, because of the recombination between V_N-type defects and excess N atoms, the ratio of the concentration of V_{Ga} to that of V_N ($[V_{Ga}]/[V_N]$) was different from that for the sample without N-implantation. Since the formation of dislocation loops requires the removal of both Ga and N atoms from the inside of the loops, the V_{Ga}-rich condition is considered to be an origin of the suppression of the formation of such secondary defects.

Comparing between Figs. 14(a) and (e), the number of the dots for the Mg-implanted sample with N-implantation was higher than that for the N-implanted sample. This fact suggests that the additional N-implantation increased not only the concentration of vacancy-type defects (Figs. 3 and 12) but also that of secondary defects. Therefore, although N sequential implantation is an effective technique for fabricating p-type GaN, there must be room to set an appropriate dosage for N depending on [Mg] and the post-implantation annealing conditions in order to increase the activation rate of Mg.

4. Summary

We used positron annihilation to study vacancy-type defects in Mg- and N-implanted GaN after UHPA. For N-implanted GaN, the major defect species in the sample before annealing was identified as V_{Ga}-type defects. After annealing at 1100°C, vacancy clusters were formed, but the size of such vacancies started to decrease above 1200°C annealing. The observed shrinkage of vacancies was attributed to recombinations between vacancy

clusters and excess N atoms. This fact suggests that one needs to anneal an ion-implanted sample at least at 1200–1300°C to obtain the effect of the sequential implantation of N on the annealing of vacancies. It was also found that a certain amount of vacancies (~10^{17} cm^{-3}) still remained even after 1400°C annealing.

For Mg-implanted GaN after annealing above 1000°C, vacancy clusters [ex. $(V_{Ga}V_N)_3$] were formed, and no large change in the defect species was observed above this annealing temperature. Above 1100°C annealing, because of the partial activation of Mg and resultant downward shift of the Fermi level position, the charge state of the vacancy clusters was changed from neutral to positive. For the sample after annealing at 1100°C, the positively charged vacancies trapped electrons excited by illumination with a photon energy above 2.6 eV. This suggests that the energy level of these defects was located 2.6 eV above the valence band. At room temperature, they acted as nonradiative recombination centers for UVL and BL bands. The thermal detrapping of electrons from the defects had multiple origins, and their full emission required about 10 h.

For Mg-implanted GaN, the major secondary defects were collapsed vacancy disks forming intrinsic dislocation loops and precipitates. The former defects were eliminated by sequential N-implantation. This was attributed to vacancy agglomeration that occurred during high temperature annealing under the V_{Ga}-rich condition. The present work revealed the trapping and detrapping of charge carriers by vacancy clusters formed by post-implantation annealing, and they would affect the electric properties of a GaN-based device fabricated by ion implantation. It was also confirmed that vacancy-type defects exist even after UHPA at 1450°C, and they play a crucial role in the formation of secondary defects and their atomic configuration.

Acknowledgements

The authors thank A. Mukaida (Tohoku University) for helping us with the PL experiments. This work was supported in part by the NEDO Program for Cross-ministerial Strategic Innovation Promotion, the MEXT Program for Research and Development of Next-Generation Semiconductor to Realize Energy-Saving Society (JPJ005357), the MEXT Program for Creation of Innovative Core Technology for Power Electronics (JPJ009777), and JSPS KAKENHI (21H01826). This research was also partially supported by the Polish National Centre for Research and Development through project TECHMATSTRATEG-III/0003/2019-00 and Polish National Science Centre through project 2018/29/B/ST5/00338.

1. J. Millán, P. Godignon, X. Perpiñà, A. Pérez-Tomás, J. Rebollo, IEEE Trans. Power Electronics, **2014**, 29, 2155.
2. F. Roccaforte, P. Fiorenza, G. Greco, R. Lo Nigro, F. Giannazzo, F. Iucolano, M. Saggio, Microelectronic Eng., **2018**, 187–188, 66.
3. T. Kimoto, Jpn. J. Appl. Phys., **2015**, 54, 040103.
4. M. Meneghini, C. De Santi, I. Abid, M. Buffolo, M. Cioni, R.A. Khadar, L. Nela, N. Zagni, A. Chini, F. Medjdoub, G. Meneghesso, G. Verzellesi, E. Zanoni, E. Matioli, J. Appl. Phys., **2021**, 130, 181101.
5. X. She, A. Q. Huang, O. Lucía, B. Ozpineci, IEEE Trans. Industrial Elect., **2017**, 64, 8193.
6. Y.H. Zhang, A. Dadgar, T. Palacios , J. Phys. D, **2018**, 51, 273001.
7. T. Kachi, T. Narita, H. Sakurai, M. Matys, K. Kataoka, K. Hirukawa, K. Sumida, M. Horita, N. Ikarashi, K. Sierakowski, M. Bockowski, J. Suda, J. Appl. Phys., **2022**, 132, 130901.
8. H. Amano, Jpn. J. Appl. Phys., **2013**, 52, 050001.
9. M. Imanishi, K. Murakami, T. Yamada, K. Kakinouchi, K. Nakamura, T. Kitamura, K. Okumura, M. Yoshimura, Y. Mori, Appl. Phys. Exp., **2019**, 12, 045508.
10. K. Grabianska, R. Kucharski, A. Puchalski, T. Sochacki, M. Bockowski, J. Cryst. Growth, **2020**, 547, 125804.
11. H. Nie, Q. Diduck, B. Alvarez, A. P. Edwards, B. M. Kayes, M. Zhang, G. Ye, T. Prunty, D. Bour, I. C. Kizilyalli, IEEE Electron Device Lett. **2014**, 35, 939.
12. T. Oka, T. Ina, Y. Ueno, J. Nishii, Appl. Phys. Exp., **2015**, 8, 054101.
13. K. Nomoto, B. Song, Z. Hu, M. Zhu, M. Qi, N. Kaneda, T. Mishima, T. Nakamura, D. Jena, H. G. Xing, IEEE Electron Device Lett. **2016**, 37, 161.

14. J. Wang, L. Cao, J. Xie, E. Beam, R. McCarthy, C. Youtsey, P. Fay, Appl. Phys. Lett., **2018**, 113, 023502.
15. R. Tanaka, S. Takashima, K. Ueno, H. Matsuyama, M. Edo, Jpn. J. Appl. Phys., **2020**, 59, SGGD02.
16. J. Liu, M. Xiao, R. Zhang, S. Pidaparthi, H. Cui, A. Edwards, M. Craven, L. Baubutr, C. Drowley, Y. Zhang, IEEE Trans. Electron Device, **2021**, 68, 2025.
17. D. Khachariya, S. Stein, W. Mecouch, M. H. Breckenridge, S. Rathkanthiwar, S. Mita, B. Moody, P. Reddy, J. Tweedie, R. Kirste, K. Sierakowski, G. Kamler, M. Bockowski, E. Kohn, S. Pavlidis, R. Collazo, Z. Sitar, Appl. Phys. Exp., **2022**, 15, 101004.
18. S. R. Stein, D. Khachariya, W. Mecouch, S. Mita, P. Reddy, J. Tweedie, K. Sierakowski, G. Kamler, M. Bockowski, E. Kohn, Z. Sitar, R. Collazo, S. Pavlidis, IEEE Trans. Electron Devices, **2023**, DOI 10.1109/ted.2023.3339592 (early access).
19. S. O. Kucheyev, J. S. Williams, S. J Pearton, Mat. Sci. Eng. Rep. **2001**, 33, 51.
20. A. Ferreyra, B. J. Li, S. Z. Wang, J. Han, J. Phys. D, **2023**, 56, 373001.
21. M. Takahashi, A. Tanaka, Y. Ando, H. Watanabe, M. Deki, M. Kushimoto, S. Nitta, Y. Honda, K. Shima, K. Kojima, S.F. Chichibu, K. J. Chen, H. Amano, Phys. Stat. Sol. (b), **2020**, 257, 1900554.
22. A. Uedono, R. Tanaka, S. Takashima, K. Ueno, M. Edo, K. Shima, K. Kojima, S.F. Chichibu, S. Ishibashi, Sci. Rep., **2021**, 11, 20660.
23. S. G. Sundaresan, M. Murthy, M.V. Rao, J. A. Schreifels, M. A. Mastro, C. R. Eddy, R. T. Holm, R. L. Henry, J. A. Freitas, E. Gomar-Nadal, R. D. Vispute, Y.-L. Tian, Semicond. Sci. Technol., **2007**, 22, 1151.
24. B. N. Feigelson, T. J. Anderson, M. Abraham, J.A. Freitas, J. K. Hite, C. R. Eddy, F.

J. Kub, J. Cryst. Growth, **2012**, 350, 21.

25. T. Niwa, T. Fujii, T. Oka, Appl. Phys. Exp., **2017**, 10, 091002.
26. S. R. Aid, T. Uneme, N. Wakabayashi, K. Yamazaki, A. Uedono, S. Matsumoto, Phys. Stat. Sol. A, **2017**, 214, 1700225.
27. H. Sakurai, M. Omori, S. Yamada, Y. Furukawa, H. Suzuki, T. Narita, K. Kataoka, M. Horita, M. Bockowski, J. Suda, T. Kachi, Appl. Phys. Lett., **2019**, 115, 142104.
28. M. H. Breckenridge, J. Tweedie, P. Reddy, Y. Guan, P. Bagheri, D. Szymanski, S. Mita, K. Sierakowski, M. Boćkowski, R. Collazo, Z. Sitar, Appl. Phys. Lett., **2021**, 118, 022101.
29. R. Krause-Rehberg, H. S. Leipner, *Positron Annihilation in Semiconductors, Solid-State Sciences* vol. 127, Springer-Verlag, Berlin, **1999**.
30. F. Tuomisto, I. Makkonen, Rev. Mod. Phys., **2013**, 85, 1583.
31. K. Saarinen, T. Laine, S. Kuisma, J. Nissila, P. Hautojarvi, L. Dobrzynski, J. M. Baranowski, K. Pakula, R. Stepniewski, M. Wojdak, A. Wysmolek, T. Suski, M. Leszczynski, I. Grzegory, S. Porowski, Phys. Rev. Lett., **1997**, 79, 3030.
32. J. Oila, V. Ranki, J. Kivioja, K. Saarinen, P. Hautojarvi, J. Likonen, J. M. Baranowski, K. Pakula, T. Suski, M. Leszczynski, I. Grzegory, Phys. Rev. B, **2001**, 63, 045205.
33. A. Uedono, S. F. Chichibu, Z. Q. Chen, M. Sumiya, R. Suzuki, T. Ohdaira, T. Mikado, T. Mukai, S. Nakamura, J. Appl. Phys., **2001**, 90, 181.
34. S.F. Chichibu, K. Shima, K. Kojima, S. Takashima, M. Edo, K. Ueno, S. Ishibashi, A. Uedono, Appl. Phys. Lett., **2018**, 112, 211901.
35. H. Iguchi, T. Narita, K. Kataoka, M. Kanechika, A. Uedono, J. Appl. Phys., **2019**, 126, 125102.
36. T. Kimura, K. Kataoka, A. Uedono, H. Amano, D. Nakamura, Appl. Phys. Exp., **2020**,

13, 085509.

37. M. Maekawa, A. Miyashita, S. Sakai, A. Kawasuso, Phys. Rev. B, **2020**, 102, 054427.
38. T. Heikkinen, J. Pavlov, T. Ceponis, E. Gaubas, M. Zając, F. Tuomisto, J. Crystal Growth, **2020**, 547, 125803.
39. F. Tuomisto, Crystals, **2022**, 12, 1112.
40. K. Sierakowski, R. Jakiela, B. Lucznik, P. Kwiatkowski, M. Iwinska, M. Turek, H. Sakurai, T. Kachi, M. Bockowski, Electronics, **2020**, 9, 1380.
41. A. Van Veen, H. Schut, M. Clement, J. M. M. de Nijs, A. Kruseman, M. R. IJpma, Appl. Surf. Sci., **1995**, 85, 216.
42. S. Ishibashi, T. Tamura, S. Tanaka, M. Kohyama, K. Terakura, Phys. Rev. B **76**, 153310 (2007).
43. P. E. Blochl, Phys. Rev. B **50**, 17953–17979 (1994).
44. J. P. Perdew, K. Burke, and M. Ernzerhof, Phys. Rev. Lett. **77**, 3865–3868 (1996).
45. S. Ishibashi and A. Uedono, J. Phys. Conf. Ser. **505**, 012010 (2014).
46. S. Ishibashi, A. Uedono, H. Kino, T. Miyake, and K. Terakura, J. Phys. Cond. Matt. **31**, 475401 (2019).
47. A. Uedono, H. Sakurai, J. Uzuhashi, T. Narita, K. Sierakowski, S. Ishibashi, S.F. Chichibu, M. Bockowski, J. Suda, T. Ohkubo, N. Ikarashi, K. Hono, T. Kachi, Phys. Stat. Sol. B, **2022**, 259, 2200183.
48. J. F. Ziegler, M. D. Ziegler, J. P. Biersack, Nucl. Instrum. Methods B, **2010**, 268, 1818.
49. A. Uedono, H. Iguchi, T. Narita, K. Kataoka, W. Egger, T. Koschine, C. Hugenschmidt, M. Dickmann, K. Shima, K. Kojima, S.F. Chichibu, S. Ishibashi, Phys. Stat. Sol. B, **2019**, 256, 1900104.

50. A. Uedono, M. Imanishi, M. Imade, M. Yoshimura, S. Ishibashi, M. Sumiya, Y. Mori, J. Cryst. Growth, **2017**, 475, 261.
51. M. A. Reshchikov, H. Hadis Morkoç, J. Appl. Phys., **2005**, 97, 061301.
52. G. Pozina, P. P. Paskov, J. P. Bergman, C. Hemmingsson, L. Hultman, B. Monemar, H. Amano, I. Akasaki, A. Usui, Appl. Phys. Lett., **2007**, 91, 221901.
53. B. Monemar, P. P. Paskov, G. Pozina, C. Hemmingsson, J. P. Bergman, T. Kawashima, H. Amano, I. Akasaki, T. Paskova, S. Figge, D. Hommel, A. Usui, Phys. Rev. Lett., **2009**, 102, 235501.
54. H. Alves, M. Bohm, A. Hofstaetter, H. Amano, S. Einfeldt, D. Hommel, D. M. Hofmann, B. K. Meyer, Phys. B, **2001**, 38, 308-310.
55. K. Shima, H. Iguchi, T. Narita, K. Kataoka, K. Kojima, A. Uedono, S.F. Chichibu, Appl. Phys. Lett., **2018**, 113, 191901.
56. J. Neugebauer, C. G. Van de Walle, Appl. Phys. Lett., **1996**, 69, 503.
57. F. Kohlrausch, Ann. Phys., **1847**, 72, 353.
58. G. Williams, D. Watts, Trans. Faraday Soc., **1970**, 66, 80.
59. M. Meneghini, G. Meneghesso, E. Zanomi, *Gallium Nitride (GaN) Physics, Devices, and Technology*, chapter 10, ed. F. Medjdoub, K. Iniewski, CRC Press, NY, **2016**.
60. K. Iwata, H. Sakurai, S. Arai, T. Nakashima, T. Narita, K. Kataoka, M. Bockowski, M. Nagao, J. Suda, T. Kachi, N. Ikarashi, J. Appl. Phys., **2020**, 127, 105106.
61. J. Uzuhashi, J. Chen, A. Kumar, W. Yi, T. Ohkubo, R. Tanaka, S. Takashima, M. Edo, K. Sierakowski, M. Bockowski, H. Sakurai, T. Kachi, T. Sekiguchi, K. Hono, J. Appl. Phys., **2022**, 131, 185701.
62. E. Kano, K. Kataoka, J. Uzuhashi, K. Chokawa, H. Sakurai, A. Uedono, T. Narita, K. Sierakowski, M. Bockowski, R. Otsuki, K. Kobayashi, Y. Itoh, M. Nagao, T. Ohkubo,

K. Hono, J. Suda, T. Kachi, N. Ikarashi, J. Appl. Phys., **2022**, 132, 065703.

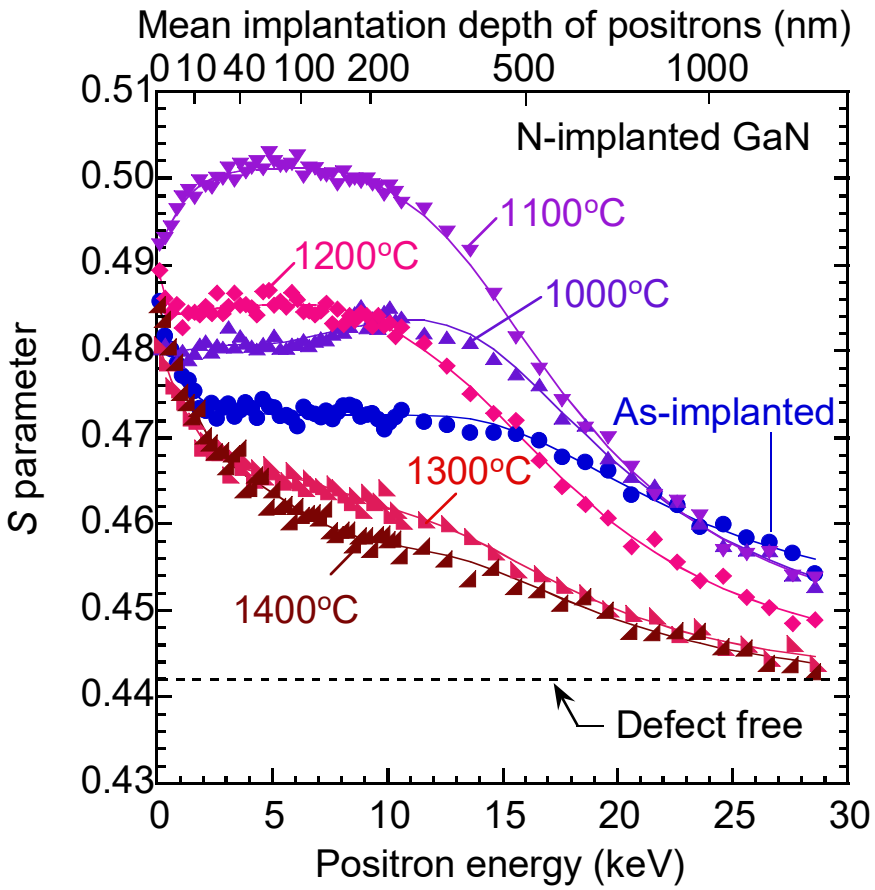

Fig. 1. *S* parameters as function of incident positron energy *E* for N-implanted GaN before and after annealing at 1000–1400°C. Solid curves are fits to experimental data. Dotted line shows *S* for annihilation of positrons from delocalized state.

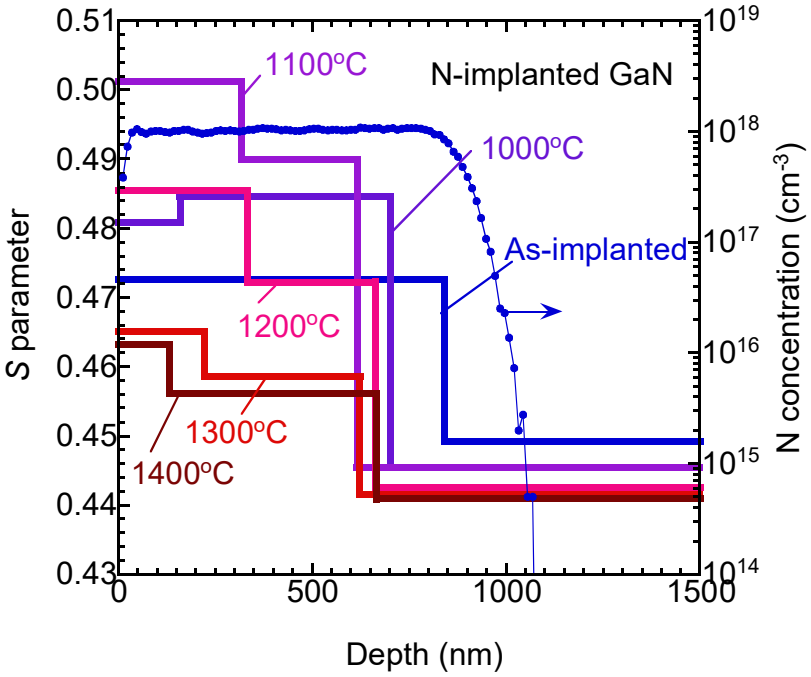

Fig. 2. Depth distributions of *S* obtained from analysis of *S*–*E* curves shown in Fig. 1 and simulated depth distribution of N implanted into GaN.

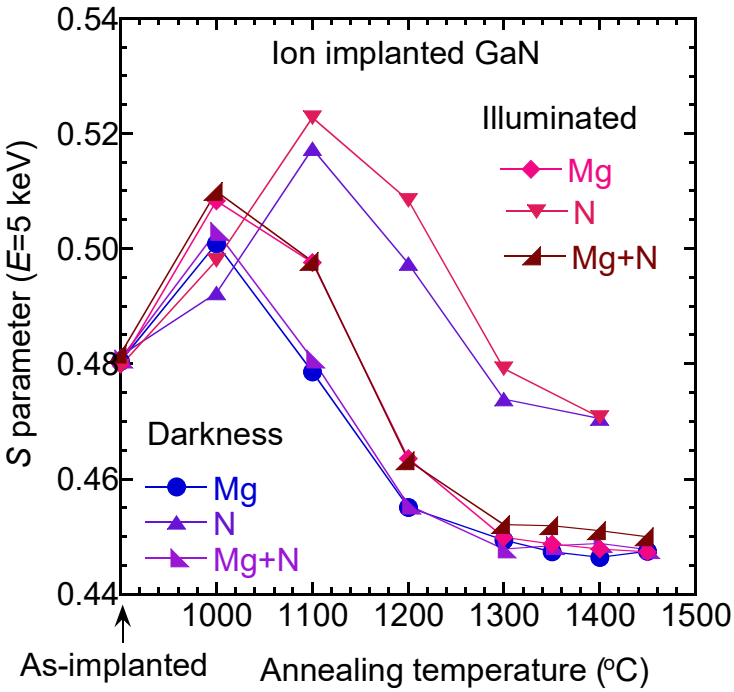

Fig. 3. *S* parameter measured at $E = 5$ keV as function of annealing temperature for Mg-implanted GaN without and with N-implantation (Mg+N). Results for N-implanted

GaN are also shown. Measurements were performed in darkness and under illumination.

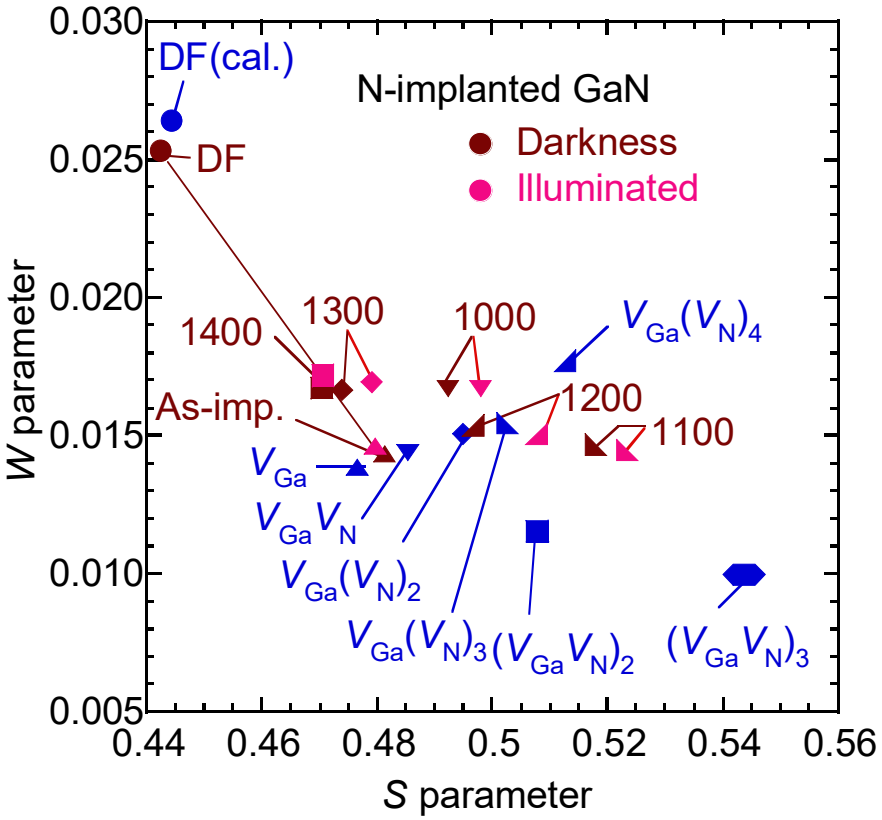

Fig. 4. *S*–*W* relationships measured in darkness (brown symbols) and under illumination (pink symbols) for N-implanted GaN before (as-imp.) and after annealing. Annealing temperatures (1000–1400°C) as shown in figure. (*S*,*W*) for un-implanted GaN is shown as "DF" (defect-free). (*S*,*W*) obtained by simulations for defect-free GaN [DF(cal.)], V_{Ga}, $V_{Ga}(V_N)_n$ (n = 1–4), $(V_{Ga}V_N)_2$, and $(V_{Ga}V_N)_3$ are shown as blue symbols.

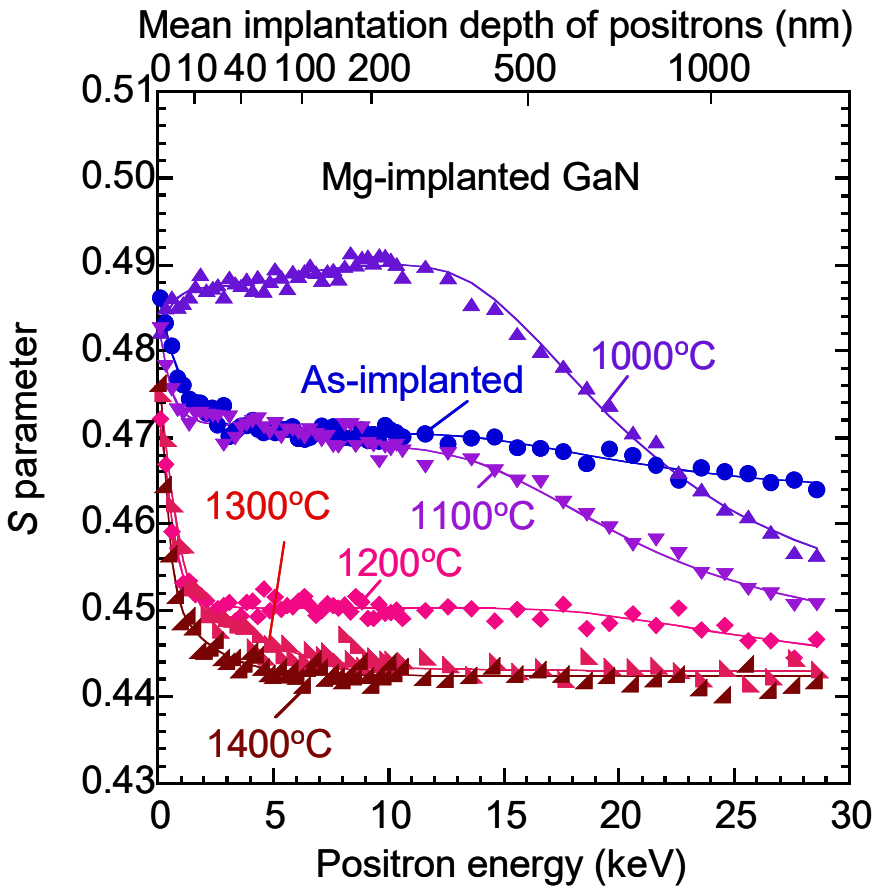

Fig. 5. *S*–*E* curves for Mg-implanted GaN before and after annealing at 1000–1400°C. Solid curves are fits to experimental data. Obtained results are shown in Fig. 6.

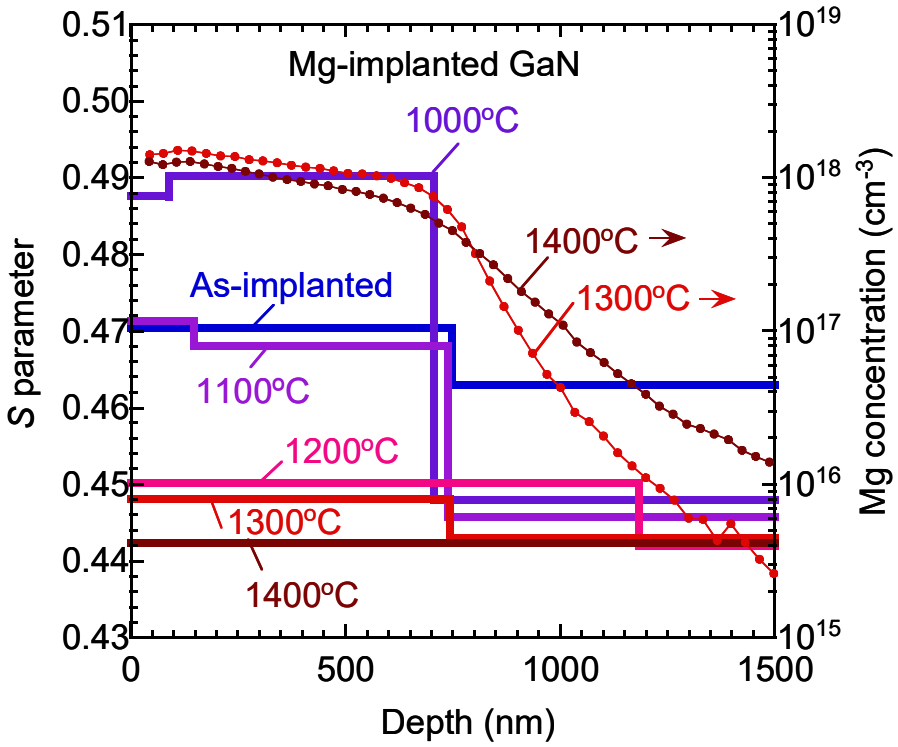

Fig. 6. Depth distributions of *S* for Mg-implanted GaN and those of Mg after annealing at 1300°C and 1400°C.

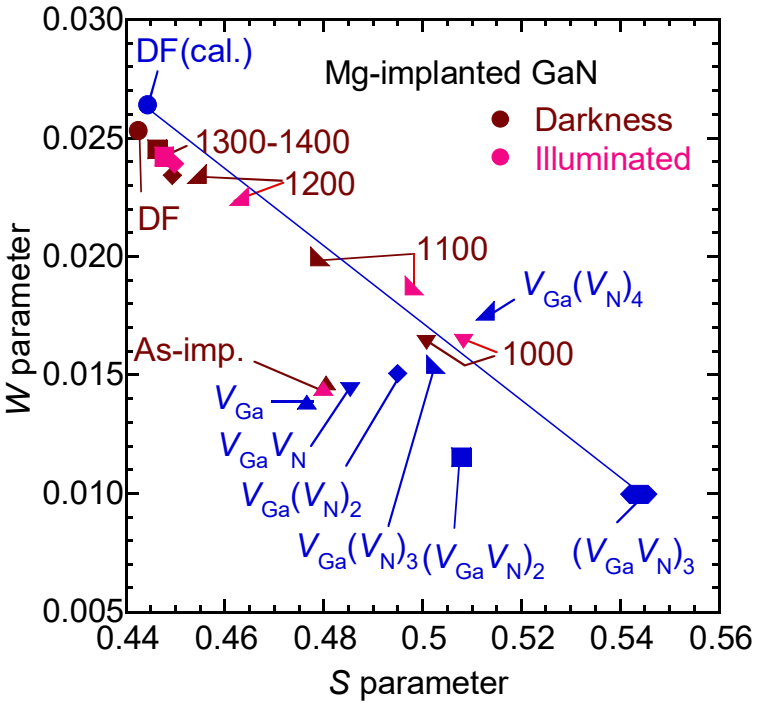

Fig. 7. *S*–*W* relationships measured in darkness and under illumination for Mg-implanted GaN (brown and pink symbols). Simulated (*S*,*W*) for vacancy-type defects are shown as blue symbols.

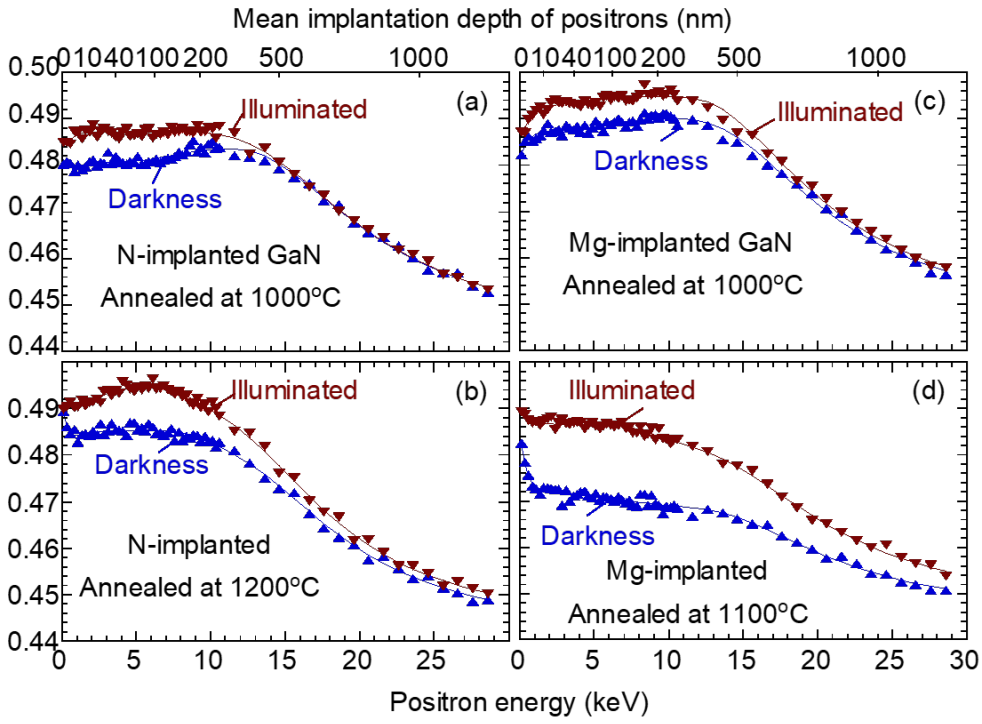

Fig. 8. *S*–*E* curves for N-implanted GaN after annealing at (a) 1000°C and (b) 1200°C, and those for Mg-implanted GaN after annealing at (c) 1000°C and (d) 1100°C. Measurements were performed in darkness and under illumination.

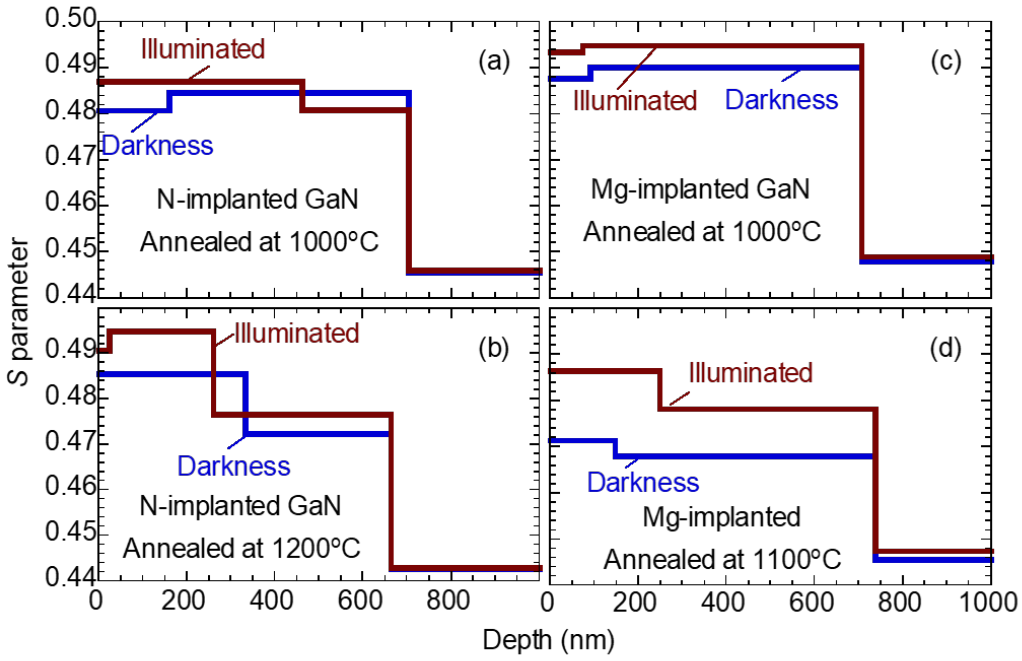

Fig. 9. Depth distribution of *S* for N-implanted GaN after annealing at (a) 1000°C and (b) 1200°C, and those for Mg-implanted GaN after annealing at (c) 1000°C and (d) 1100°C.

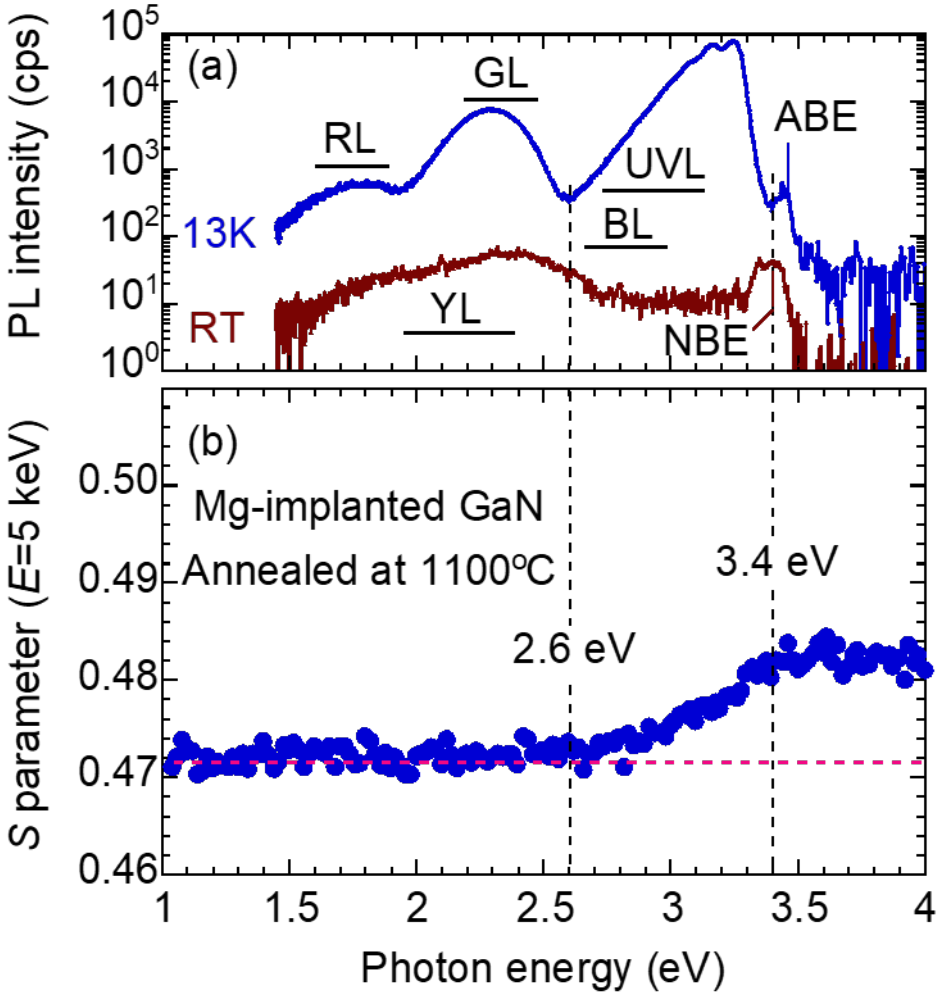

Fig. 10. (a) PL intensities measured at 13 K and room temperature (RT) and (b) *S* measured at $E = 5$ keV as function of photon energy for Mg-implanted GaN annealed at 1100°C. Luminescence peaks corresponding to acceptor bonded exciton (ABE) and near-band-edge (NBE) emissions are shown in figure.

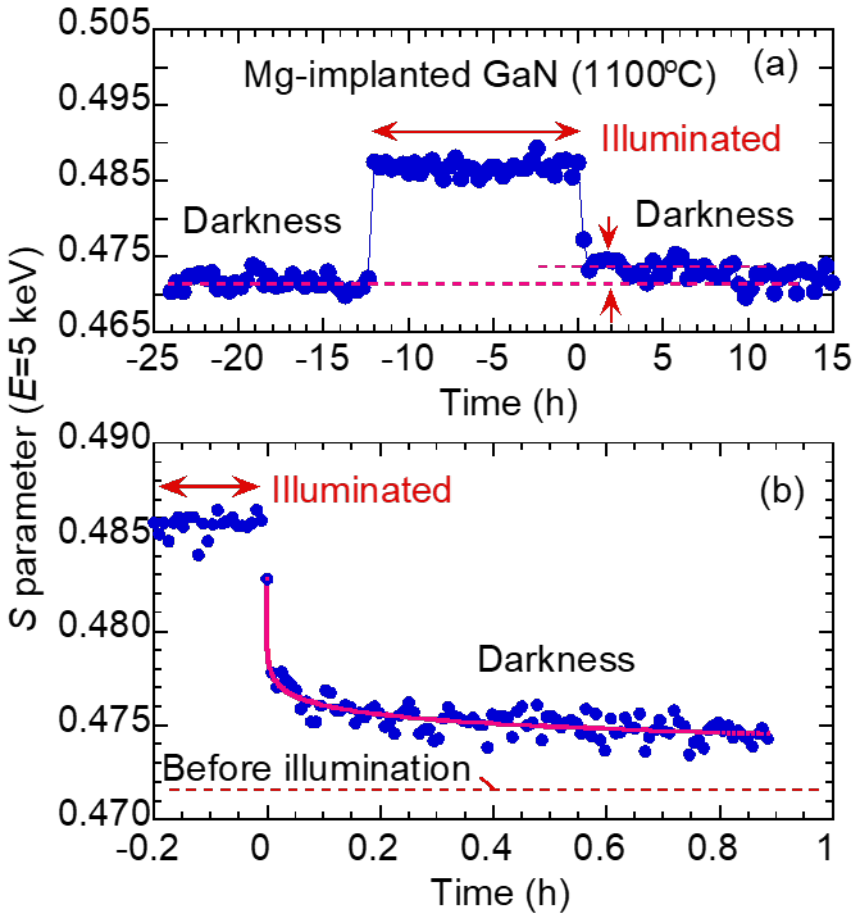

Fig. 11. Time dependence of *S* measured in (a) wide and (b) narrow time ranges for Mg-implanted GaN annealed at 1100°C after illumination. Incident energy of positrons was fixed at E = 5 keV. Dotted lines correspond to *S* before illumination. Solid line is fit to experimental data.

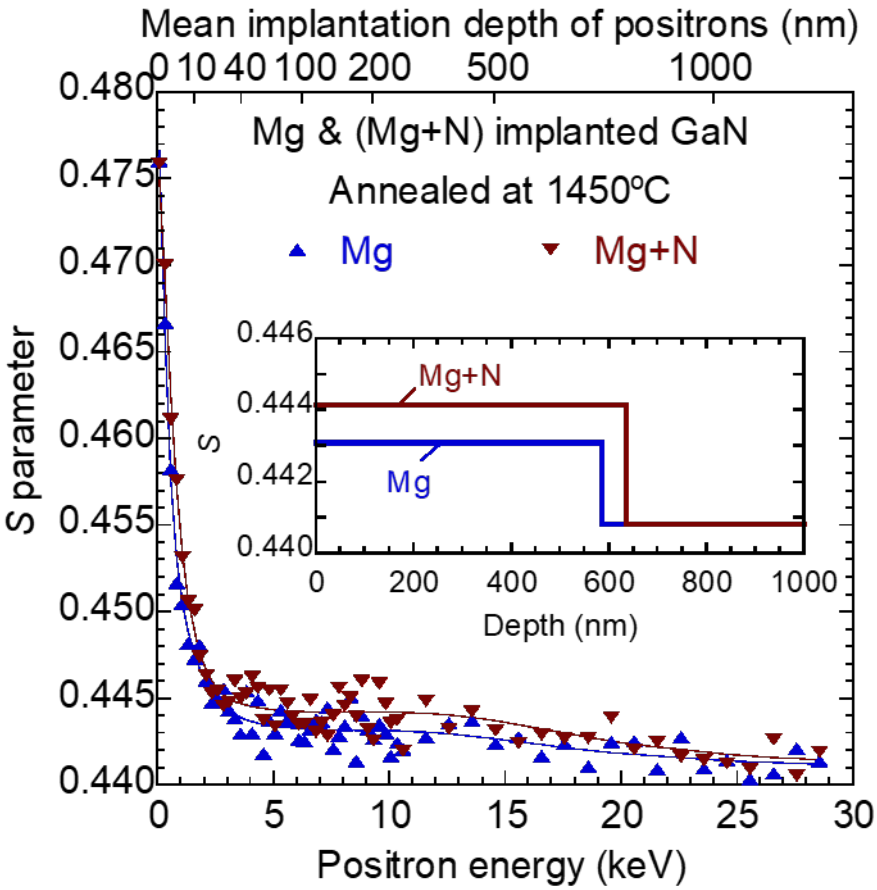

Fig. 12. *S*–*E* curves for Mg-implanted GaN with and without N-implantation after annealing at 1450°C. Solid curves are fits to experimental data. Inset shows obtained depth distributions of *S*.

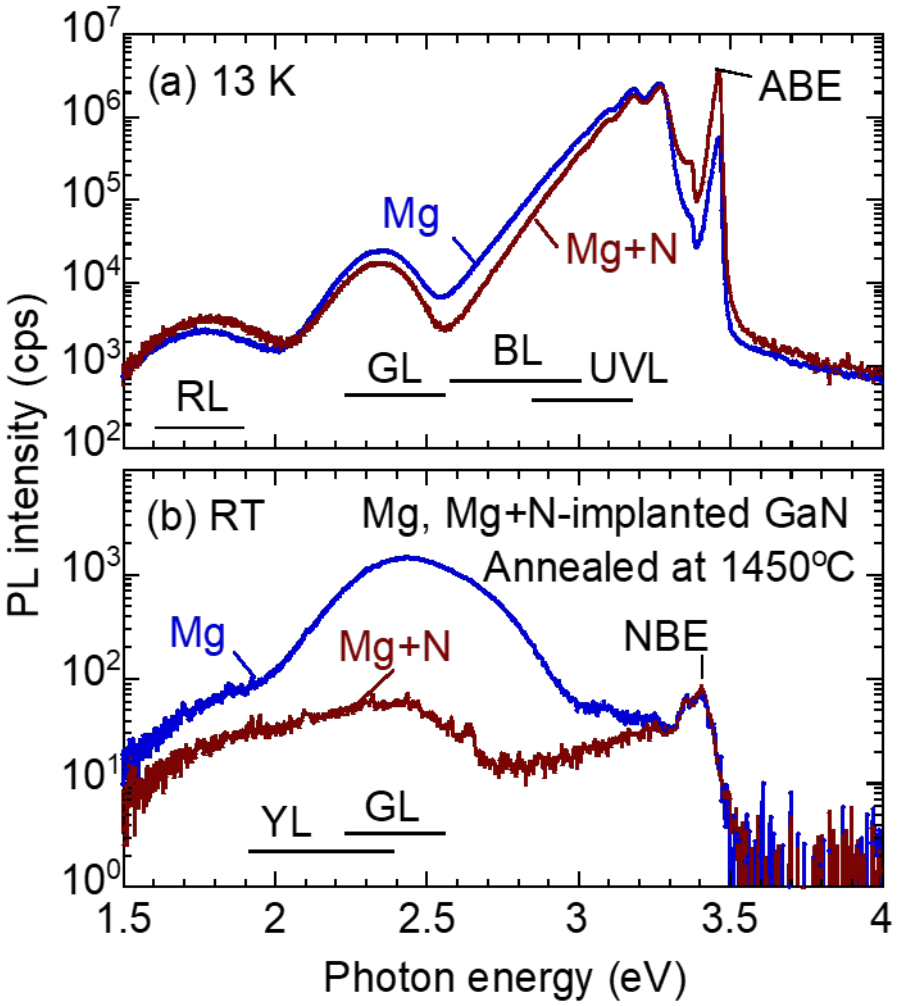

Fig. 13. PL spectra measured at (a) 13K and (b) RT for Mg-implanted GaN with and without N-implantation after annealing at 1450°C.

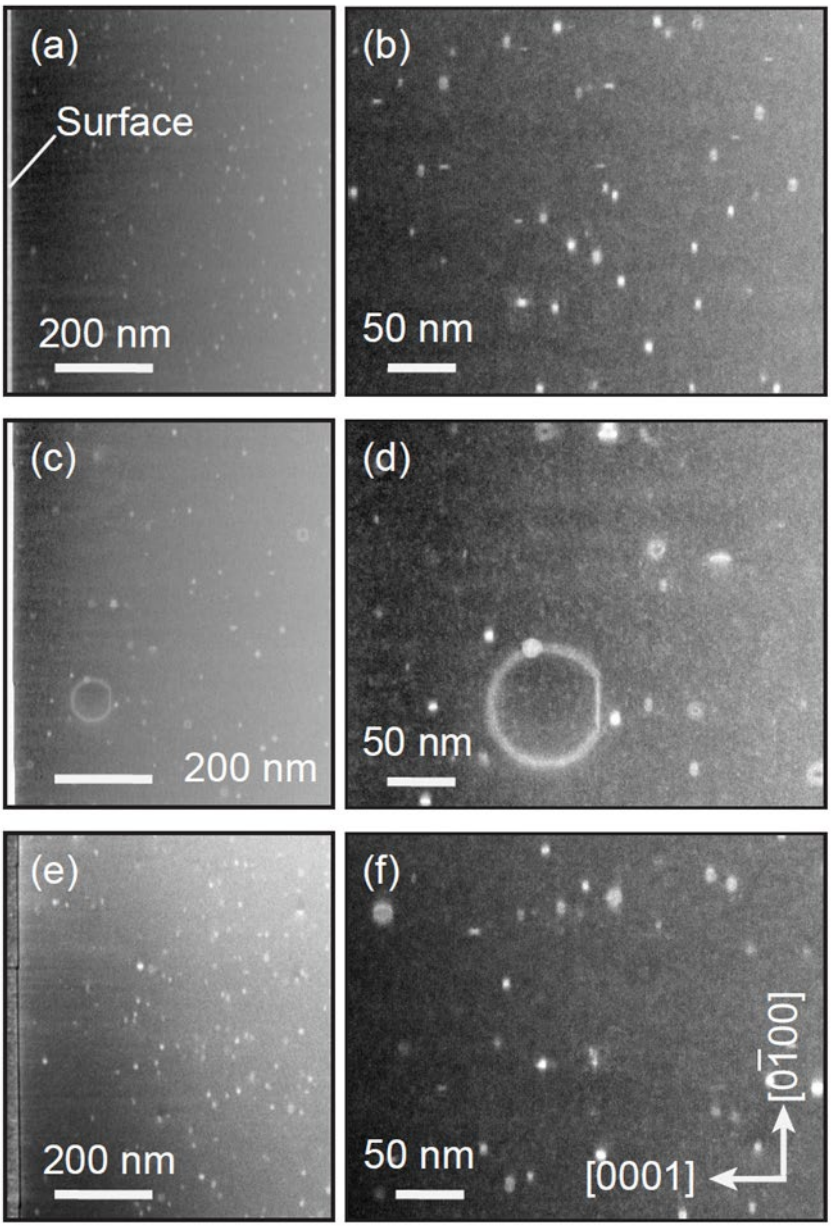

Fig. 14. LAADF-STEM images of (a) N-implanted GaN, (c) Mg-implanted GaN, and (e) Mg-implanted GaN with N-implantation. Their magnified images are shown in (b), (d), and (f), respectively. All samples were annealed at 1400°C.